



Article

Investigations on the Carrier Mobility of Cs₂NaFeCl₆ Double Perovskites

Jiyuan Xing^{1,2}, Yiting Zhao^{1,2}, Wei-Yan Cong^{1,2,*}, Chengbo Guan², Zhongchen Wu^{1,2} , Dong Liu^{1,2} 
and Ying-Bo Lu^{1,2,*}¹ Shandong Key Laboratory of Optical Astronomy and Solar-Terrestrial Environment, Institute of Space Sciences, Shandong University, Weihai 264209, China; jienaxumi@mail.sdu.edu.cn (J.X.)² School of Space Science and Physics, Shandong University, Weihai 264209, China* Correspondence: cong_wy@sdu.edu.cn (W.-Y.C.); lyb@sdu.edu.cn (Y.-B.L.);
Tel.: +86-131-8110-4093 (W.-Y.C.); +86-138-6316-0610 (Y.-B.L.)

Abstract: Double perovskite materials have gradually become widely studied due to their potential applications in solar cells and other optoelectronic devices. We take Cs₂NaFeCl₆ as an example to investigate the carrier mobility with respect to the acoustic phonon and the optical phonon scattering mechanisms. By considering the deformation potential, carrier effective mass, and bulk modulus, the longitudinal acoustic (LA) phonon-determined mobilities for electrons and holes in Cs₂NaFeCl₆ are found to be $\mu_e = 2886.08 \text{ cm}^2 \text{ v}^{-1} \text{ s}^{-1}$ and $\mu_h = 39.09 \text{ cm}^2 \text{ v}^{-1} \text{ s}^{-1}$, respectively. The optical scattering mechanism involves calculating the Fröhlich coupling constant, dielectric constant, and polaron mass to determine the multiple polar optical (PO) phonon-scattering-determined mobilities, resulting in $\mu_e = 279.25 \text{ cm}^2 \text{ v}^{-1} \text{ s}^{-1}$ and $\mu_h = 21.29 \text{ cm}^2 \text{ v}^{-1} \text{ s}^{-1}$, respectively. By combining both interactions, the total electron mobility and hole mobility are determined to be $254.61 \text{ cm}^2 \text{ v}^{-1} \text{ s}^{-1}$ and $13.78 \text{ cm}^2 \text{ v}^{-1} \text{ s}^{-1}$, respectively. The findings suggest that the polarization of both electrons and ions, small coupling constant, and bulk modulus in Cs₂NaFeCl₆'s lattice make PO scattering a significant contribution to carrier mobility in this specific double perovskite, highlighting the importance of considering this in enhancing the optoelectronic properties of Cs₂NaFeCl₆ and other double perovskites.

Keywords: Cs₂NaFeCl₆ double perovskites; carrier mobility; stability; LA phonon scattering; PO phonon scattering



Citation: Xing, J.; Zhao, Y.; Cong, W.-Y.; Guan, C.; Wu, Z.; Liu, D.; Lu, Y.-B. Investigations on the Carrier Mobility of Cs₂NaFeCl₆ Double Perovskites. *Crystals* **2024**, *14*, 547. <https://doi.org/10.3390/cryst14060547>

Received: 17 May 2024
Revised: 4 June 2024
Accepted: 8 June 2024
Published: 12 June 2024



Copyright: © 2024 by the authors. Licensee MDPI, Basel, Switzerland. This article is an open access article distributed under the terms and conditions of the Creative Commons Attribution (CC BY) license (<https://creativecommons.org/licenses/by/4.0/>).

1. Introduction

Solar cells, such as silicon solar cells, organic solar cells, and perovskite solar cells (PSCs), are considered highly promising energy sources due to their renewable and clean properties [1–5]. Research on halide perovskite materials has significantly advanced in recent years, with the power conversion efficiency (PCE) increasing from an initial value of 3.8% to a remarkable 26.41% in just 15 years [6,7]. Furthermore, the theoretical PCE of PSCs can potentially reach 31%, surpassing the theoretical limit of 29% for silicon solar cells. These exceptional optoelectronic properties of halide perovskites stem from their adjustable band gap, strong absorption, and high carrier mobility [8–11]. However, the investigation of organic–inorganic perovskites, such as MAPbBr₃ and MAPbI₃, has revealed certain drawbacks like instability and Pb toxicity, which limit their practical applications. In response, extensive research efforts are being directed towards identifying new halide perovskites that exhibit improved stability and environmental compatibility, while retaining their exceptional optoelectronic properties. Consequently, interest in double perovskites is steadily growing among researchers. Double perovskites with the formula A₂B'B''X₆ are created by substituting the B-site (Pb²⁺) cation with a lead-free combination of monovalent (B') and trivalent (B'') cation pairs. Researchers have demonstrated that the double perovskites Cs₂AgBiX₆ (X = Cl, Br, I) have potential for optoelectronic applications through

the precise control of surface defects [12]. For instance, $\text{Cs}_2\text{AgBiCl}_6$ has shown promise in high energy radiation detection [13,14] and as a white light emitter [15]. Various strategies can be employed to adjust the physical properties of double perovskites. For instance, Cu doping has been shown to enhance the photoelectric performance of $\text{Cs}_2\text{AgSbCl}_6$ [16]. The band gap of double perovskites can also be modulated by changing A cations, as has been demonstrated theoretically [17]. Additionally, studies have successfully synthesized $(\text{CH}_3\text{NH}_3)_2\text{AgBiI}_6$ with high stability in air, making it a viable option for tandem solar cells [18].

Despite advancements, the efficiency of double perovskite solar cells still lags behind that of traditional perovskite solar cells. Semiconductors' optoelectronic properties are influenced by various factors, including the absorption efficiency, quantum efficiency, and carrier mobility [19,20]. Among these factors, the carrier mobility, which refers to the transport efficiency of light-generated electron/hole pairs, plays a crucial role in determining the power conversion efficiency (PCE) of solar cells. Several studies have indicated that CsPbBr_3 has an electron mobility of around $1000 \text{ cm}^2 \text{ v}^{-1} \text{ s}^{-1}$, which is comparable to that of Si [21,22]. Additionally, the mobility of MAPbI_3 can reach up to $800 \text{ cm}^2 \text{ v}^{-1} \text{ s}^{-1}$, while MASnI_3 boasts a mobility exceeding $2000 \text{ cm}^2 \text{ v}^{-1} \text{ s}^{-1}$ [23,24]. These high mobilities play a crucial role in enhancing the optoelectronic performance of perovskite solar cells (PSCs). Conversely, $\text{Cs}_2\text{AgBiBr}_6$ double perovskite demonstrates a relatively low electron/hole mobility of $16.7/14.2 \text{ cm}^2 \text{ v}^{-1} \text{ s}^{-1}$ [25], leading to subpar photovoltaic performance [26,27]. As a result, extensive research efforts are being conducted to enhance the transport properties of double perovskites. For example, some studies have shown that impurity doping or adjusting the composition of $\text{Cs}_2\text{AgInCl}_6$ can modulate the carrier mobility, resulting in the development of novel double perovskites [28].

Recently, a new double perovskite, $\text{Cs}_2\text{NaFeCl}_6$, was successfully synthesized, displaying environmental stability, thermal stability, and thermochromic cyclic stability [29,30]. The exciton-binding energy of $\text{Cs}_2\text{NaFeCl}_6$ is only 20 meV at 80 K, facilitating the separation of light-induced electron/hole pairs and leading to high optoelectronic efficiency [31]. However, the experimentally measured carrier mobility of $\text{Cs}_2\text{NaFeCl}_6$ at room temperature is initially low. To enhance the transport properties, various methods have been implemented. For example, Ag doping has been found to elevate the electron mobility from $1.06 \text{ cm}^2 \text{ v}^{-1} \text{ s}^{-1}$ to $15.3 \text{ cm}^2 \text{ v}^{-1} \text{ s}^{-1}$. Additionally, the incorporation of Ag substantially boosts the carrier diffusion length from 3.7 nm to 311 nm. Notably, the measured hole carrier mobility is unexpectedly higher than the electron carrier mobility in $\text{Cs}_2\text{NaFeCl}_6$, which differs from other perovskites [32]. In order to enhance the optoelectronic performance of $\text{Cs}_2\text{NaFeCl}_6$ and other double perovskites for practical applications, a comprehensive understanding of their electronic properties is crucial. It is imperative to investigate how carriers move within the crystalline structure of $\text{Cs}_2\text{NaFeCl}_6$ and identify the scattering mechanism that dictates the upper limit of mobility. Only by clarifying these aspects can we develop precise strategies to enhance the transport properties of $\text{Cs}_2\text{NaFeCl}_6$. To date, no research has addressed these critical factors.

Therefore, the acoustic and optical phonon scattering mechanisms in $\text{Cs}_2\text{NaFeCl}_6$ were investigated using a semi-empirical model of a longitudinal acoustic (LA) phonon and polar optical (PO) phonon. It was observed that the mobilities of electrons/holes in $\text{Cs}_2\text{NaFeCl}_6$ are primarily influenced by PO phonon scattering, attributed to its polarization of both electrons and ions, weak coupling, and small bulk modulus. These insights can potentially aid in enhancing the transport properties of $\text{Cs}_2\text{NaFeCl}_6$ and other double perovskites.

2. Methods

2.1. First Principle Calculations

First principle simulations were carried out using VASP 5.2 software to study the double perovskite material $\text{Cs}_2\text{NaFeCl}_6$, with the crystal structure (file 2001471) obtained from the CCDC database [33]. Density functional theory was utilized [34] to analyze the crystal structure, bulk modulus, carrier effective mass, and dielectric constant of the

$\text{Cs}_2\text{NaFeCl}_6$ perovskite. The k-point mesh was set at $4 \times 4 \times 4$ for lattice relaxation and $8 \times 8 \times 8$ for electronic structure calculations. Spin-orbit coupling (SOC) was considered due to the heavy elements in $\text{Cs}_2\text{NaFeCl}_6$ perovskite. The Projector-Augmented Wave (PAW) method with a cutoff energy of 400 eV was used to calculate the electronic wave functions. The convergence thresholds for the total energy and force in the iterative process are 10^{-4} eV per atom and 0.01 eV per Å, respectively.

2.2. Mobility Calculations

As carriers traverse the vibrating lattice of solid materials, they undergo continuous collisions with lattice atoms or ionized impurities, leading to scattering that alters their trajectories and ultimately determines the upper limit of their carrier mobility. Various factors contribute to these scattering interactions, including acoustic phonon scattering and optical phonon scattering. At low temperatures, LA phonon scattering predominantly influences the acoustic phonon scattering. Specifically, the LA phonon induces changes in the band edges, resulting in potential disturbances and subsequent carrier scattering. The carrier mobility derived from the LA phonon model can be represented by Equation (1) [35].

$$\mu_\alpha = \frac{2\sqrt{2}\pi e\hbar^4 C_\alpha}{3(k_B T)^{3/2} m_\alpha^{*5/2} E_\alpha^2} \quad (1)$$

where e , \hbar , and k_B represent the unit charge, the reduced Planck constant, and the Boltzmann constant, respectively. T denotes the temperature, while C_α stands for the bulk modulus, and E_α is the volume deformation potential.

When the carriers are scattered by optical phonons, the polarized electric field accompanied by longitudinal optical vibration impacts a strong coupling interaction on electrons, known as Fröhlich action [36]. Therefore, the mobility determined by polaron LO phonon scattering is referred to as the PO-determined carrier mobility in the subsequent sections. The degree of polarization is denoted by the electron-phonon coupling constant α [37], which can be calculated using the following formula:

$$\alpha = \frac{1}{4\pi\epsilon_0} \frac{1}{2} \left(\frac{1}{\epsilon_\infty} - \frac{1}{\epsilon_s} \right) \frac{e^2}{\hbar\Omega} \left(\frac{2m_b\Omega}{\hbar} \right)^{1/2} \quad (2)$$

where ϵ_∞ is the high-frequency dielectric constant, ϵ_s is the static dielectric constant, Ω is the optical branch frequency, m_b is the effective carrier mass, and ϵ_0 is the vacuum dielectric constant. The PO-determined carrier mobility can be described using Equation (3) [38].

$$\mu_e = \frac{4}{3\pi^{1/2}} \frac{e}{m_p \alpha \omega_{LO}} G \left(\frac{\hbar\omega_{LO}}{k_B T} \right) \left(\frac{k_B T}{\hbar\omega_{LO}} \right)^{1/2} \exp \left(\frac{\hbar\omega_{LO}}{k_B T} \right) \quad (3)$$

where G is the degeneracy factor, which usually varies between 0.8 and 2, and we set this value as 1 in this work [38]. m_p is the polaron mass, and ω_{LO} is the optical branch frequency.

3. Results and Discussions

3.1. Geometric Structures

The relaxed $\text{Cs}_2\text{NaFeCl}_6$ supercell is depicted in Figure 1a, with lattice parameters of 10.33 Å. The bond lengths of Cs-Cl, Na-Cl, and Fe-Cl are measured at 3.66 Å, 2.86 Å, and 2.31 Å, respectively. The structure of $\text{Cs}_2\text{NaFeCl}_6$ adheres to the standard cubic double perovskite lattice, with the Na-Cl-Fe bond angles measuring 180.00° .

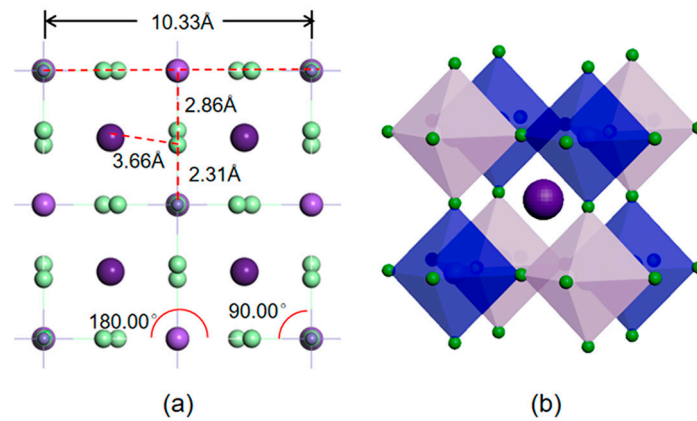


Figure 1. (a) The geometric structures and (b) metal octahedron frameworks of $\text{Cs}_2\text{NaFeCl}_6$. The dark purple, light purple, light green, and dark blue balls represent Cs, Na, Cl, and Fe atoms, respectively. The numbers in (a) denote the bond lengths and the bond angles.

The stability of a perovskite can be evaluated using the tolerance factor t , which is defined in Equation (4).

$$t = \frac{R_A + R_X}{\sqrt{2}(R_B + R_X)} \quad (4)$$

where R_A , R_B , and R_X represent the radii of the constituent ions in ABX_3 perovskites. It is important to note that in double perovskite materials with the $\text{A}_2\text{B}'\text{B}''\text{X}_6$ structure, R_B in Equation (4) can be calculated using the average atomic radii of the monovalent (B') and trivalent (B'') cation pairs. To assess the stability of the $\text{Cs}_2\text{NaFeCl}_6$ lattice further, the tolerance factor t can be determined using the following equation:

$$t = \frac{\langle \text{Cs} - \text{Cl} \rangle}{\sqrt{2} \langle \text{X} - \text{Cl} \rangle_{\text{avg}}} \quad (5)$$

where $\langle \text{Cs} - \text{Cl} \rangle$ represents the interatomic distance of Cs and Cl atoms, namely, the Cs-Cl bond length. Meanwhile, $\langle \text{X} - \text{Cl} \rangle_{\text{avg}}$ equals the average value of the Na-Cl and Fe-Cl bond lengths. A cubic structure is considered stable when the value of t falls between 0.9 and 1.0; otherwise, the structure may distort to enhance bonding interactions. The results for $\text{Cs}_2\text{NaFeCl}_6$ are presented in Table 1, revealing a tolerance factor of 1.00, indicating the stability of the cubic phase. This suggests that the $\text{Cs}_2\text{NaFeCl}_6$ lattice is isotropic with no lattice distortion, a finding supported by the identification of Raman active vibration modes. The polarization characteristics of these modes imply $Fm\text{-}3m$ symmetry for the $\text{Cs}_2\text{NaFeCl}_6$ lattice, indicating an average ordered distribution of Fe and Na atoms throughout the lattice [39].

Table 1. The lattice parameter, the bond lengths, and the tolerance factor t of $\text{Cs}_2\text{NaFeCl}_6$.

a (Å)	Cs-Cl (Å)	Na-Cl (Å)	Fe-Cl (Å)	t
10.33	3.66	2.86	2.31	1.00

3.2. LA Phonon-Determined Carrier Mobility

As per Equation (1), detailed in Section 2.2, various factors must be determined prior to calculating the mobility of LA phonons. Of these factors, the effective mass of carriers holds paramount importance. Utilizing first principle calculations, we acquired the band structure of $\text{Cs}_2\text{NaFeCl}_6$, depicted in Figure 2b. To ensure precision, we accounted for the SOC effect in our calculations. Figure 2b illustrates that both the valence band maximum (VBM) and the conduction band minimum (CBM) are situated at the Γ point, constituting a direct band gap with a value of 1.09 eV. This implies that the electron momentum can

remain constant during the transition process, leading to enhanced luminous efficiency and making it well suited for the fabrication of photoelectric devices. The effective masses of the electron and hole are obtained by fitting the formula of $m^* = \hbar^2 / (\partial^2 E(k) / \partial k^2)$ on the VBM and CBM, which are $m_h^* = 2.22 m_0$ and $m_e^* = 0.42 m_0$, respectively. This shows that the hole's effective mass in $\text{Cs}_2\text{NaFeCl}_6$ is about 5 times larger than the electron's effective mass, indicating that the electrons are more dominant than the hole in the carrier migration. In addition to effective masses, the bulk modulus and volume deformation potential play crucial roles in the LA phonon model. The bulk modulus characterizes the connection between the volumetric strain and average stress. The calculated bulk modulus of $\text{Cs}_2\text{NaFeCl}_6$ is 20.32 GPa, a similar value to that of other halide perovskites [40]. The bulk modulus is determined by analyzing the second derivative of the system's energy in relation to volume variations, thus showing sensitivity to the lattice phonon modes. In the case of halide perovskites, a smaller bulk modulus is linked to the presence of low-frequency phonon modes within the inorganic lattice [41]. We believe that the small bulk modulus observed in $\text{Cs}_2\text{NaFeCl}_6$ suggests that electrons mainly interact with these low-frequency lattice phonons, effectively reducing the charge reorganization.

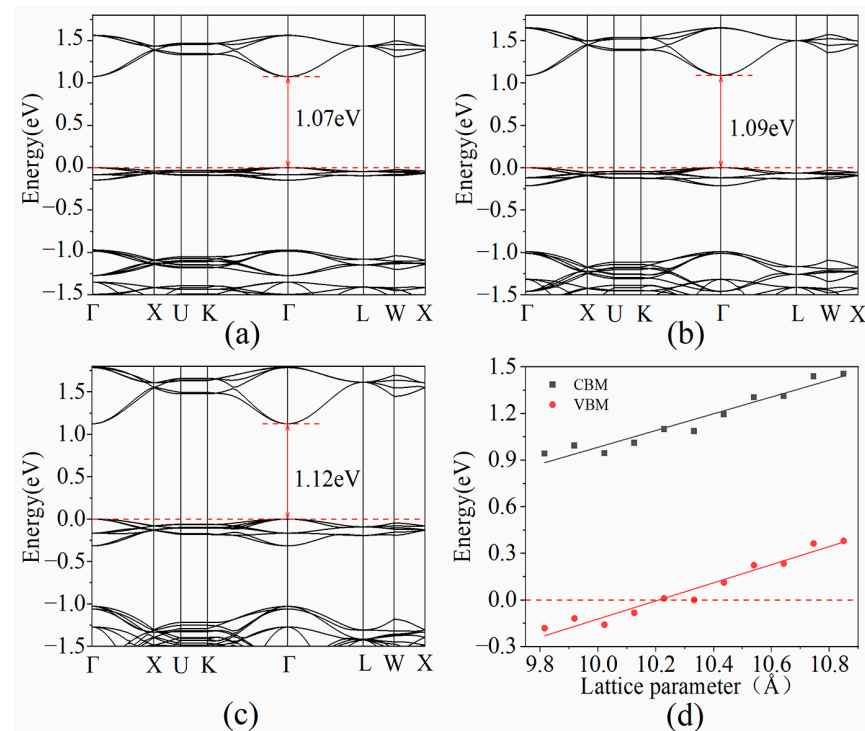


Figure 2. Band structures of (a) 1.05-strained, (b) unstrained, and (c) 0.95-strained $\text{Cs}_2\text{NaFeCl}_6$ supercells, respectively. (d) The variation in VBM and CBM after strain is applied.

With the introduction of strain and the subsequent vibration of the crystal lattice, the band edges also change accordingly, giving birth to the deformation potential. To simulate the lattice vibration under applied strain, we changed the lattice size of $\text{Cs}_2\text{NaFeCl}_6$ manually in the range of a [0.95, 1.05] strain, incrementing by 0.01 to create eleven strained configurations. Each configuration was optimized with fixed lattice parameters while allowing for relaxation of all interior atomic positions. Figure 3 displays some of the optimized structures.

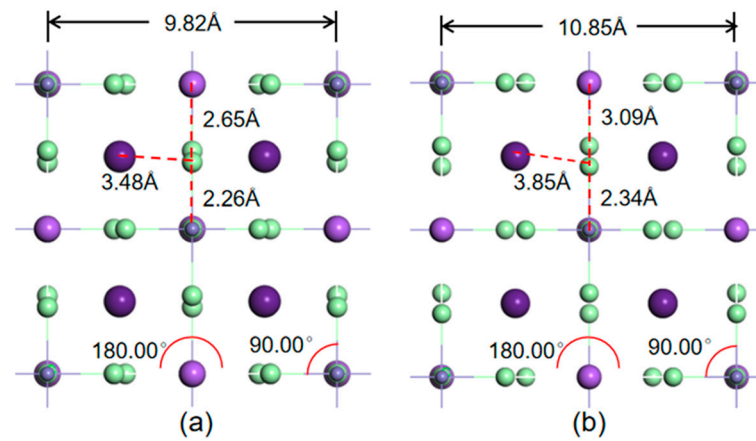


Figure 3. Optimized geometric structures of (a) 0.95-strained and (b) 1.05-strained $\text{Cs}_2\text{NaFeCl}_6$ supercells. Numbers in all figures represent the bond lengths and the bond angles, respectively. The dark purple, light purple, light green, and dark blue balls represent Cs, Na, Cl, and Fe atoms, respectively.

Figure 2a,c show the band structures of $\text{Cs}_2\text{NaFeCl}_6$ during stretching and compression, respectively. Both structures keep the direct band gap, and the band gaps of 1.05-strained and 0.95-strained $\text{Cs}_2\text{NaFeCl}_6$ are 1.07 eV and 1.12 eV, respectively. The variation in band gaps is caused by changes in the band edges under strain. The lattice vibrations introduced by the LA phonon alter the positions of the band edges, resulting in deformation potentials of $\text{Cs}_2\text{NaFeCl}_6$. To obtain a more accurate position of the band edges, we conducted band alignment among these strained $\text{Cs}_2\text{NaFeCl}_6$ systems using the Cs-6s orbit as the base energy level. The results are depicted in Figure 2d. The volume deformation potentials are calculated using the formula $E = \partial E_{\text{edge}} / \partial \ln V$ and are $E_e = 1.94$ eV and $E_h = 2.08$ eV for the electron and hole, respectively. The calculated deformation potentials are listed in Table 2.

Table 2. The calculated effective mass, bulk modulus, volume deformation potentials, and LA-dominated carrier mobility of $\text{Cs}_2\text{NaFeCl}_6$ under room temperature.

Carrier	m^* (m_0)	$C\alpha$ (GPa)	E (eV)	μ ($\text{cm}^2 \text{v}^{-1} \text{s}^{-1}$)
Electron	0.42	20.32	1.94	2886.08
Hole	2.22	20.32	2.08	39.09

m^* means the effective carrier mass.

Using these parameters obtained above, the carrier mobilities at room temperature ($T = 300$ K) were determined to be $\mu_e = 2886.08 \text{ cm}^2 \text{v}^{-1} \text{s}^{-1}$ and $\mu_h = 39.09 \text{ cm}^2 \text{v}^{-1} \text{s}^{-1}$ for LA phonon interactions. It was observed that in the LA phonon-dominant mode, the electron mobility significantly exceeds that of the hole, which is attributed to the smaller effective mass of electrons.

3.3. PO Phonon-Determined Carrier Mobility

The interaction between carriers and the macroscopic electric field generated by the LO phonons in polar semiconductors is referred to as the Fröhlich interaction. Equation (2) allows us to determine the electron–phonon coupling constant α by considering the high-frequency dielectric constant, the static dielectric constant, the effective mass of the carrier, and the characteristic phonon angular frequency.

The dielectric constant is the main parameter representing the dielectric or polarization properties of a material under the static electric field. From the first principle calculations, we obtained the contributions from electrons and ions to the dielectric function of $\text{Cs}_2\text{NaFeCl}_6$ separately, which are shown in Figure 4. Using the high-frequency dielectric constant relationship $\epsilon_\infty = \epsilon_e |_{\omega=0}$ and the static dielectric constant relationship $\epsilon_s = \epsilon_e |_{\omega=0} + \epsilon_i |_{\omega=0}$, the high-frequency dielectric constant and the static dielectric constant

were derived as $\epsilon_\infty = 16.42$ and $\epsilon_s = 24.51$, respectively. These obtained permittivities are rather large, indicating that the electrostatic shielding effect inside the $\text{Cs}_2\text{NaFeCl}_6$ lattice is strong. Some studies proposed that the $\Delta\epsilon = \epsilon_s - \epsilon_\infty$ is determined by the polarization of electrons and ions. The value of $\Delta\epsilon$ for $\text{Cs}_2\text{NaFeCl}_6$ in this work is 8.09, which is significantly higher than typical non-polar semiconductor materials. For example, the theoretical/experimental $\Delta\epsilon$ values of GaAs, AlAs, and GaP are 1.6/2.3, 1.9/1.9 and 1.8/2.1, respectively [35]. That is, this large value of $\Delta\epsilon$ indicates strong polarization of both electrons and ions for the $\text{Cs}_2\text{NaFeCl}_6$ double perovskites. Therefore, the coupling constant α , calculated using these aforementioned parameters, is relatively small, indicating that the electron–phonon coupling generated by the LO phonon in $\text{Cs}_2\text{NaFeCl}_6$ is a weak coupling effect.

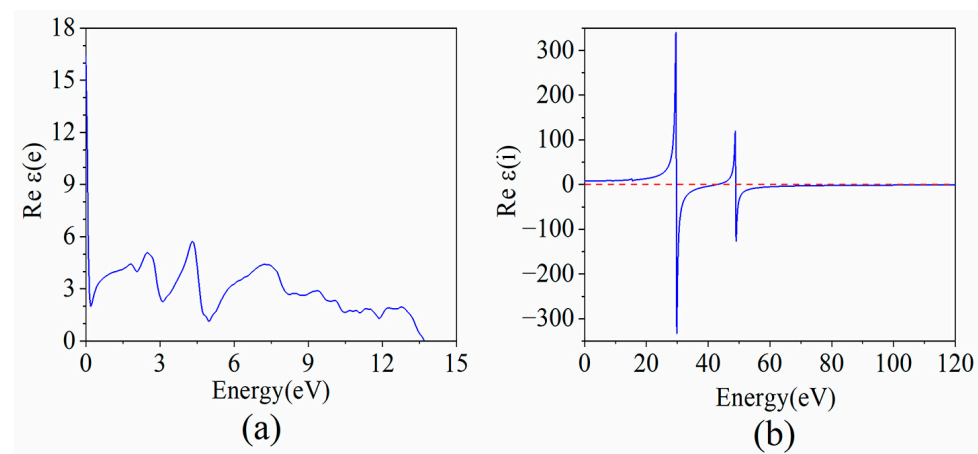


Figure 4. (a) The electronic and (b) ionic contributions to the dielectric function of $\text{Cs}_2\text{NaFeCl}_6$, respectively.

Previous reports have indicated the presence of multiple optical phonon branches in the Raman spectra of $\text{Cs}_2\text{NaFeCl}_6$, suggesting that there is not a single characteristic angular frequency for the optical phonon. In order to gain a comprehensive understanding of the mobility of $\text{Cs}_2\text{NaFeCl}_6$, we calculated the coupling constants for each optical phonon branch with multiple frequencies, rather than simply average these frequencies for each optical branch. At room temperature, the wave numbers of these multiple optical phonons are approximately 55.80 cm^{-1} , 163.80 cm^{-1} , and 292.00 cm^{-1} , corresponding to 1.67 THz, 4.91 THz, and 8.75 THz, respectively [39]. In polar and ionic crystals, the combination of electrons in the conduction band and the resulting lattice distortions form what is known as a polaron. The movement of charge carriers can be simplified as the movement of these polarons. Consequently, the masses of the polarons play a vital role in understanding their transport properties, which can be determined using the following formula:

$$m_p = m^* (1 + \alpha/6) \quad (6)$$

The polaron masses can be determined through the Fröhlich interaction with the corresponding charge carriers [42]. By utilizing Equations (2) and (6), we were able to derive the distinct coupling constants and corresponding polaron masses for different optical phonon branches, which are presented in Table 3.

It can be seen from Table 3 that both the coupling constants of the electron and hole have low values, which is ascribed to the fact that the effective masses of the electron and hole are relatively small, and the values of the static dielectric constant and high-frequency dielectric constant are relatively large, leading to an insignificant Fröhlich interaction in $\text{Cs}_2\text{NaFeCl}_6$. Notably, the coupling constant of the hole is significantly larger than that of the electron. By employing Equation (7), we calculated the total polaronic phonon-determined mobility by considering multiple optical phonon branches, where the reciprocity of the total mobility is equal to the sum of the reciprocities of the mobilities for each branch.

Table 3. The calculated electron–phonon coupling constants α , the polaron masses, and the carrier mobilities, determined by the PO phonons of $\text{Cs}_2\text{NaFeCl}_6$ with multiple optical vibrations.

Carrier	ω (THz)	α	m_p (m_0)	μ ($\text{cm}^2 \text{v}^{-1} \text{s}^{-1}$)
Electron	1.67	0.58	0.46	1194.25
	4.91	0.34	0.44	709.42
	8.75	0.25	0.44	749.62
	Total			279.25
Hole	1.67	1.33	2.72	88.08
	4.91	0.78	2.51	54.21
	8.75	0.58	2.44	58.27
	Total			21.29

$$\frac{1}{\mu_{PO}} = \frac{1}{\mu_{\omega 1}} + \frac{1}{\mu_{\omega 2}} + \frac{1}{\mu_{\omega 3}} + \dots \quad (7)$$

Using Equations (3) and (7), we were able to calculate the electron and hole mobilities for each optical branch, as well as the total mobility within the polar phonon model, which are also listed in Table 3. As can be seen, the total mobilities for the electrons and holes are $\mu_e = 279.25 \text{ cm}^2 \text{v}^{-1} \text{s}^{-1}$ and $\mu_h = 21.29 \text{ cm}^2 \text{v}^{-1} \text{s}^{-1}$, respectively. Similar to the result discussed above, the mobility of the electrons is still larger than that of the holes in the PO phonon-dominated modes. These analyses reveal that the deformation potential, bulk modulus, and dielectric constant have similar effects on the mobility of both electrons and holes. However, the effective mass of a hole is five times that of an electron. Based on Equations (1)–(3) discussed above, we can conclude that the mobility of an electron is much larger than that of a hole. Our results are consistent with the experimental and theoretical observations on the mobility of most perovskites [24,25,28]. Moreover, among the mobilities obtained from the LA scattering model and PO scattering model, we found that the mobility that was dominated by PO phonon scattering aligns more closely with the experimentally measured mobility of $\text{Cs}_2\text{NaFeCl}_6$ double perovskites. Therefore, it can be inferred that the carrier mobility in $\text{Cs}_2\text{NaFeCl}_6$ is predominantly determined by the PO phonon model.

3.4. The Dominant Factor for Mobility

Based on those analyses of the acoustic phonon and the optical phonon scattering for carrier mobility, the total carrier mobility of $\text{Cs}_2\text{NaFeCl}_6$ can be calculated via the following equation:

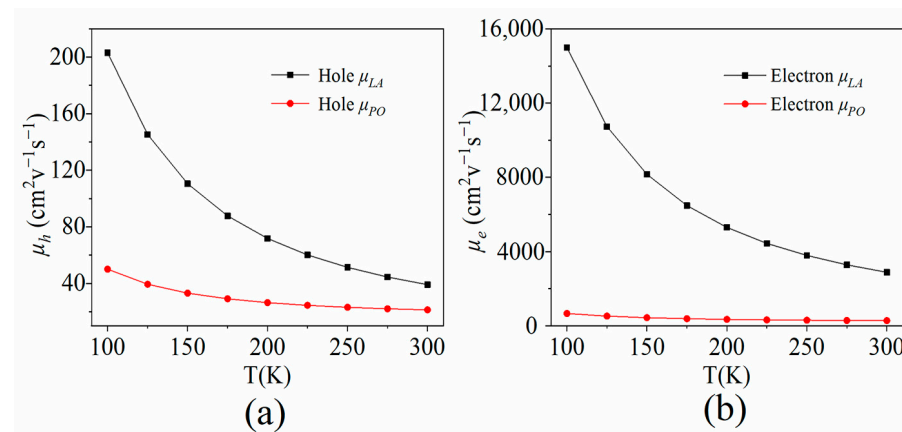
$$\frac{1}{\mu_{\text{Total}}} = \frac{1}{\mu_{LA}} + \frac{1}{\mu_{PO}} \quad (8)$$

Table 4 presents the electron mobility calculation for $\text{Cs}_2\text{NaFeCl}_6$, yielding a value of $254.61 \text{ cm}^2 \text{v}^{-1} \text{s}^{-1}$, which is dominated by PO phonon scattering. The reason for the dominant contribution from the PO scattering is that the relatively small electron effective mass of $\text{Cs}_2\text{NaFeCl}_6$ leads to a more profound Fröhlich coupling interaction in the polarization field generated by optical lattice waves. In contrast, the hole mobility in $\text{Cs}_2\text{NaFeCl}_6$ is calculated to be $13.78 \text{ cm}^2 \text{v}^{-1} \text{s}^{-1}$, with predominant contributions from PO phonon scattering and noticeable effects from LA phonon scattering. This indicates that the low coupling constant also affects the dominant role of optical phonon scattering in the hole mobility of $\text{Cs}_2\text{NaFeCl}_6$. The relatively larger effective mass of the hole is more susceptible to the low frequency phonon and is more easily affected by the bulk modulus, thus showing a mobility that is dominated by PO phonon scattering, with a considerable effect from LA phonon scattering.

Table 4. The total carrier mobility (μ_{Total}) of $\text{Cs}_2\text{NaFeCl}_6$ under room temperature.

Carrier	μ_{LA} ($\text{cm}^2 \text{v}^{-1} \text{s}^{-1}$)	μ_{PO} ($\text{cm}^2 \text{v}^{-1} \text{s}^{-1}$)	μ_{Total} ($\text{cm}^2 \text{v}^{-1} \text{s}^{-1}$)
Electron	2886.08	279.25	254.61
Hole	39.09	21.29	13.78

Our theoretical results are basically in agreement with the experimentally observed data and can provide elaborate explanations for their intrinsic mechanism. Furthermore, we applied the same methodology to analyze the variation in carrier mobility of $\text{Cs}_2\text{NaFeCl}_6$ with temperature, which is important for the real applications of this material. Figure 5 illustrates that within the temperature range of 100–300 K, the mobilities of both electrons and holes decrease with the increase in temperature. Moreover, the mobilities of electrons and holes dominated by LA phonon scattering are always higher than that determined by PO phonon scattering. This suggests that PO phonon scattering continues to dominate the carrier mobility of $\text{Cs}_2\text{NaFeCl}_6$ in the 100–300 K range.

**Figure 5.** The mobilities of $\text{Cs}_2\text{NaFeCl}_6$ dominated by LA and PO scattering for (a) μ_e and (b) μ_h in the temperature range of 100 K–300 K, respectively.

Previous research has shown that an acoustic phonon limits the mobility of non-polar semiconductors, while an optical phonon is the primary source of carrier scattering in polar semiconductors [43,44]. The high $\Delta\epsilon$ value suggests that $\text{Cs}_2\text{NaFeCl}_6$ is highly polar and is prone to PO phonon scattering. As a result, applying an electric field to $\text{Cs}_2\text{NaFeCl}_6$ causes distortion in the electron cloud and shifts in ion positions, ultimately resulting in carrier scattering. Recent studies have analyzed the polarity of organic–inorganic hybrid perovskites through theoretical and experimental approaches, suggesting that their polarity is influenced by factors such as composition, processing, and environment. This dynamic nature of polarity can impact the carrier mobility in various manners, highlighting the need for additional research on $\text{Cs}_2\text{NaFeCl}_6$ and other double perovskites.

4. Conclusions

In summary, this study focused on the theoretical investigation of the carrier mobility of $\text{Cs}_2\text{NaFeCl}_6$. By analyzing the electronic, dielectric, and elastic properties of the cubic double perovskite structure of $\text{Cs}_2\text{NaFeCl}_6$, we aimed to identify the key factors that influence the carrier mobility in this unique material. The carrier mobility of $\text{Cs}_2\text{NaFeCl}_6$ was calculated considering both acoustic phonon and optical phonon scattering mechanisms. The deformation potential was determined by applying strain to the original $\text{Cs}_2\text{NaFeCl}_6$ supercell, resulting in values of 2.08 eV for the VBM and 1.94 eV for the CBM. Using the calculated carrier effective mass and bulk modulus, we finally obtained the LA phonon-determined mobilities of $\text{Cs}_2\text{NaFeCl}_6$ for electrons and holes with values of $\mu_e = 2886.08 \text{ cm}^2 \text{v}^{-1} \text{s}^{-1}$ and $\mu_h = 39.09 \text{ cm}^2 \text{v}^{-1} \text{s}^{-1}$, respectively. In a model of the optical scattering mechanism, the Fröhlich coupling constant ascribed for

the electron–phonon coupling, the dielectric constant, and the polaron mass were calculated, and then, the multiple PO phonon-scattering-determined mobilities of $\text{Cs}_2\text{NaFeCl}_6$ were obtained accordingly for electrons and holes, with values of $\mu_e = 279.25 \text{ cm}^2 \text{ v}^{-1} \text{ s}^{-1}$ and $\mu_h = 21.29 \text{ cm}^2 \text{ v}^{-1} \text{ s}^{-1}$, respectively. Finally, by combining the acoustic phonon and optical phonon interactions, we obtained the electron mobility and the hole mobility of $254.61 \text{ cm}^2 \text{ v}^{-1} \text{ s}^{-1}$ and $13.78 \text{ cm}^2 \text{ v}^{-1} \text{ s}^{-1}$, respectively. According to our calculated results, we revealed that due to the polarization of both electrons and ions in $\text{Cs}_2\text{NaFeCl}_6$, the PO scattering makes significant contributions to the carrier mobility of this double perovskite. More importantly, this gives indications for us that the double perovskites show complicated scattering mechanisms for the electrons and holes, which should be considered to further promote the optoelectronic properties of $\text{Cs}_2\text{NaFeCl}_6$ and other double perovskites.

Author Contributions: Conceptualization, Y.-B.L. and J.X.; methodology, J.X.; software, Y.Z.; validation, Z.W. and D.L.; formal analysis, C.G., Y.Z. and J.X.; investigation, J.X.; writing—original draft preparation, J.X.; writing—review and editing, Y.-B.L. and W.-Y.C. All authors have read and agreed to the published version of the manuscript.

Funding: This research was funded by the Natural Science Foundation of Shandong Province, grant number ZR2020MA067, and the National Natural Science Foundation of China, grant number 42173045, 11504202.

Data Availability Statement: The original contributions presented in the study are included in the article/supplementary material, further inquiries can be directed to the corresponding author/s.

Acknowledgments: This work is supported by the Physical-Chemical Materials Analytical & Testing Center of Shandong University at Weihai.

Conflicts of Interest: The authors declare no conflicts of interest.

References

1. Li, Q.; Liu, Y.; Guo, S.; Zhou, H. Solar energy storage in the rechargeable batteries. *Nano Today* **2017**, *16*, 46–60. [[CrossRef](#)]
2. Liu, X.; Yuan, Y.; Liu, J.; Liu, B.; Chen, X.; Ding, J.; Han, X.; Deng, Y.; Zhong, C.; Hu, W. Utilizing solar energy to improve the oxygen evolution reaction kinetics in zinc–air battery. *Nat. Commun.* **2019**, *10*, 4767. [[CrossRef](#)] [[PubMed](#)]
3. Zhao, J.; Xu, Z.; Zhou, Z.; Xi, S.; Xia, Y.; Zhang, Q.; Huang, L.; Mei, L.; Jiang, Y.; Gao, J.; et al. A Safe Flexible Self-Powered Wristband System by Integrating Defective MnO_{2-x} Nanosheet-Based Zinc-Ion Batteries with Perovskite Solar Cells. *ACS Nano* **2021**, *15*, 10597–10608. [[CrossRef](#)] [[PubMed](#)]
4. Yang, Y.; Hoang, M.T.; Bhardwaj, A.; Wilhelm, M.; Mathur, S.; Wang, H. Perovskite solar cells based self-charging power packs: Fundamentals, applications and challenges. *Nano Energy* **2022**, *94*, 106910. [[CrossRef](#)]
5. Melskens, J.; van de Loo, B.W.H.; Macco, B.; Black, L.E.; Smit, S.; Kessels, W.M.M. Passivating Contacts for Crystalline Silicon Solar Cells: From Concepts and Materials to Prospects. *IEEE J. Photovolt.* **2018**, *8*, 373–388. [[CrossRef](#)]
6. Zhou, J.; Tan, L.; Liu, Y.; Li, H.; Liu, X.; Li, M.; Wang, S.; Zhang, Y.; Jiang, C.; Hua, R.; et al. Highly efficient and stable perovskite solar cells via a multifunctional hole transporting material. *Joule* **2024**, *8*, 1–16. [[CrossRef](#)]
7. Kojima, A.; Teshima, K.; Shirai, Y.; Miyasaka, T. Organometal Halide Perovskites as Visible-Light Sensitizers for Photovoltaic Cells. *J. Am. Chem. Soc.* **2009**, *131*, 6050–6051. [[CrossRef](#)] [[PubMed](#)]
8. Liu, M.; Johnston, M.B.; Snaith, H.J. Efficient planar heterojunction perovskite solar cells by vapour deposition. *Nature* **2013**, *501*, 395–398. [[CrossRef](#)] [[PubMed](#)]
9. Wu, L.; Lu, P.; Li, Y.; Sun, Y.; Wong, J.; Yang, K. First-principles characterization of two-dimensional $(\text{CH}_3(\text{CH}_2)_3\text{NH}_3)_2(\text{CH}_3\text{NH}_3)_{n-1}\text{Ge}_n\text{I}_{3n+1}$ perovskite. *J. Mater. Chem. A* **2018**, *6*, 24389–24396. [[CrossRef](#)]
10. Najim, A.; Hartiti, B.; Absike, H.; Tchognia Nkuissi, H.J.; Labrim, H.; Fadili, S.; Thevenin, P.; Ertugrul, M. Theoretical investigation of structural, electronic, and optical properties of halide cubic perovskite $\text{CsPbBr}_{3-x}\text{I}_x$. *Mater. Sci. Semicond. Process.* **2022**, *141*, 106442. [[CrossRef](#)]
11. Kanoun, M.B.; Goumri-Said, S. Insights into the impact of Mn-doped inorganic CsPbBr_3 perovskite on electronic structures and magnetism for photovoltaic application. *Mater. Today Energy* **2021**, *21*, 100796. [[CrossRef](#)]
12. Yang, B.; Chen, J.; Yang, S.; Hong, F.; Sun, L.; Han, P.; Pullerits, T.; Deng, W.; Han, K. Lead-Free Silver-Bismuth Halide Double Perovskite Nanocrystals. *Angew. Chem. Int. Ed.* **2018**, *57*, 5359–5363. [[CrossRef](#)] [[PubMed](#)]
13. Pan, W.; Wu, H.; Luo, J.; Deng, Z.; Ge, C.; Chen, C.; Jiang, X.; Yin, W.-J.; Niu, G.; Zhu, L.; et al. $\text{Cs}_2\text{AgBiBr}_6$ single-crystal X-ray detectors with a low detection limit. *Nat. Photonics* **2017**, *11*, 726–732. [[CrossRef](#)]

14. Steele, J.A.; Pan, W.; Martin, C.; Keshavarz, M.; Debroye, E.; Yuan, H.; Banerjee, S.; Fron, E.; Jonckheere, D.; Kim, C.W.; et al. Photophysical Pathways in Highly Sensitive Cs₂AgBiBr₆ Double-Perovskite Single-Crystal X-ray Detectors. *Adv. Mater.* **2018**, *30*, 1804450. [[CrossRef](#)]
15. Luo, J.; Wang, X.; Li, S.; Liu, J.; Guo, Y.; Niu, G.; Yao, L.; Fu, Y.; Gao, L.; Dong, Q.; et al. Efficient and stable emission of warm-white light from lead-free halide double perovskites. *Nature* **2018**, *563*, 541–545. [[CrossRef](#)]
16. Yu, G.; Xue, S.; Yin, R.; Wu, Q.; Gao, T.; Song, Y.; Wang, R.; Cong, W.Y.; Guan, C.; Lu, Y.B. How the Copper Dopant Alters the Geometric and Photoelectronic Properties of the Lead-Free Cs₂AgSbCl₆ Double Perovskite. *Adv. Theory Simul.* **2021**, *4*, 2100142. [[CrossRef](#)]
17. Yin, R.; Yu, G.; Cong, W.-Y.; Guan, C.; Li, J.; Lu, Y.-B. Modulation Effect Generated by A Cations in Hybrid A₂BB'X₆ Double Halogen Perovskite Materials. *ACS Appl. Mater. Interfaces* **2020**, *12*, 44798–44804. [[CrossRef](#)]
18. Cheng, P.; Wu, T.; Li, Y.; Jiang, L.; Deng, W.; Han, K. Combining theory and experiment in the design of a lead-free ((CH₃NH₃)₂AgBiI₆) double perovskite. *New J. Chem.* **2017**, *41*, 9598–9601. [[CrossRef](#)]
19. Gao, W.; Ran, C.; Xi, J.; Jiao, B.; Zhang, W.; Wu, M.; Hou, X.; Wu, Z. High-Quality Cs₂AgBiBr₆ Double Perovskite Film for Lead-Free Inverted Planar Heterojunction Solar Cells with 2.2% Efficiency. *ChemPhysChem* **2018**, *19*, 1696–1700. [[CrossRef](#)]
20. Igbari, F.; Wang, R.; Wang, Z.-K.; Ma, X.-J.; Wang, Q.; Wang, K.-L.; Zhang, Y.; Liao, L.-S.; Yang, Y. Composition Stoichiometry of Cs₂AgBiBr₆ Films for Highly Efficient Lead-Free Perovskite Solar Cells. *Nano Lett.* **2019**, *19*, 2066–2073. [[CrossRef](#)]
21. Jacoboni, C.; Canali, C.; Ottaviani, G.; Quaranta, A.A. A review of some charge transport properties of silicon. *Solid-State Electron.* **1977**, *20*, 77–89.
22. Stoumpos, C.C.; Malliakas, C.D.; Peters, J.A.; Liu, Z.; Sebastian, M.; Im, J.; Chasapis, T.C.; Wibowo, A.C.; Chung, D.Y.; Freeman, A.J.; et al. Crystal Growth of the Perovskite Semiconductor CsPbBr₃: A New Material for High-Energy Radiation Detection. *Cryst. Growth Des.* **2013**, *13*, 2722–2727. [[CrossRef](#)]
23. Valverde-Chávez, D.A.; Ponseca, C.S.; Stoumpos, C.C.; Yartsev, A.; Kanatzidis, M.G.; Sundström, V.; Cooke, D.G. Intrinsic femtosecond charge generation dynamics in single crystal CH₃NH₃PbI₃. *Energy Environ. Sci.* **2015**, *8*, 3700–3707. [[CrossRef](#)]
24. Stoumpos, C.C.; Malliakas, C.D.; Kanatzidis, M.G. Semiconducting Tin and Lead Iodide Perovskites with Organic Cations: Phase Transitions, High Mobilities, and Near-Infrared Photoluminescent Properties. *Inorg. Chem.* **2013**, *52*, 9019–9038. [[CrossRef](#)] [[PubMed](#)]
25. Leveille, J.; Volonakis, G.; Giustino, F. Phonon-Limited Mobility and Electron–Phonon Coupling in Lead-Free Halide Double Perovskites. *J. Phys. Chem. Lett.* **2021**, *12*, 4474–4482. [[CrossRef](#)] [[PubMed](#)]
26. Longo, G.; Mahesh, S.; Buizza, L.R.V.; Wright, A.D.; Ramadan, A.J.; Abdi-Jalebi, M.; Nayak, P.K.; Herz, L.M.; Snaith, H.J. Understanding the Performance-Limiting Factors of Cs₂AgBiBr₆ Double-Perovskite Solar Cells. *ACS Energy Lett.* **2020**, *5*, 2200–2207. [[CrossRef](#)]
27. Sirtl, M.T.; Ebadi, F.; van Gorkom, B.T.; Ganswindt, P.; Janssen, R.A.J.; Bein, T.; Tress, W. The Bottlenecks of Cs₂AgBiBr₆ Solar Cells: How Contacts and Slow Transients Limit the Performance. *Adv. Opt. Mater.* **2021**, *9*, 2100202. [[CrossRef](#)]
28. Jain, M.; Bhumla, P.; Kumar, M.; Bhattacharya, S. Lead-Free Alloyed Double Perovskites: An Emerging Class of Materials for Optoelectronic Applications. *J. Phys. Chem. C* **2022**, *126*, 6753–6760. [[CrossRef](#)]
29. Ji, F.; Klarbring, J.; Zhang, B.; Wang, F.; Wang, L.; Miao, X.; Ning, W.; Zhang, M.; Cai, X.; Bakht, B.; et al. Remarkable Thermochromism in the Double Perovskite Cs₂NaFeCl₆. *Adv. Opt. Mater.* **2023**, *12*, 2301102. [[CrossRef](#)]
30. Li, W.; Rahman, N.U.; Xian, Y.; Yin, H.; Bao, Y.; Long, Y.; Yuan, S.; Zhang, Y.; Yuan, Y.; Fan, J. Regulation of the order–disorder phase transition in a Cs₂NaFeCl₆ double perovskite towards reversible thermochromic application. *J. Semicond.* **2021**, *42*, 072202. [[CrossRef](#)]
31. Armer, M.; Dörflinger, P.; Weis, A.; Büchner, C.; Gottscholl, A.; Höcker, J.; Frank, K.; Nusser, L.; Sirtl, M.T.; Nickel, B.; et al. Low Temperature Optical Properties of Novel Lead-Free Cs₂NaFeCl₆ Perovskite Single Crystals. *Adv. Photon Res.* **2023**, *4*, 2300017. [[CrossRef](#)]
32. Xian, Y.; Yin, H.; Bao, Y.; Xiao, Y.; Yuan, S.; Rahman, N.U.; Yuan, Y.; Zhang, Y.; Meng, X.; Jin, S.; et al. Engineered Electronic Structure and Carrier Dynamics in Emerging Cs₂Ag_xNa_{1-x}FeCl₆ Perovskite Single Crystals. *J. Phys. Chem. Lett.* **2020**, *11*, 9535–9542. [[PubMed](#)]
33. Kresse, G.; Furthmüller, J. Efficient iterative schemes for ab initio total-energy calculations using a plane-wave basis set. *Phys. Rev. B* **1996**, *54*, 11169–11186. [[CrossRef](#)] [[PubMed](#)]
34. Kresse, G.; Joubert, D. From ultrasoft pseudopotentials to the projector augmented-wave method. *Phys. Rev. B* **1999**, *59*, 1758–1775. [[CrossRef](#)]
35. Su, Y.; Wang, H.; Shi, L.-B.; Wang, Y.-Z.; Liu, Q.; Qian, P. An investigation on carrier transport behavior of tetragonal halide perovskite: First-principles calculation. *Mater. Sci. Semicond. Process.* **2022**, *150*, 106836. [[CrossRef](#)]
36. Hendry, E.; Wang, F.; Shan, J.; Heinz, T.F.; Bonn, M. Electron transport in TiO₂ probed by THz time-domain spectroscopy. *Phys. Rev. B* **2004**, *69*, 081101. [[CrossRef](#)]
37. Steele, J.A.; Puech, P.; Keshavarz, M.; Yang, R.; Banerjee, S.; Debroye, E.; Kim, C.W.; Yuan, H.; Heo, N.H.; Vanacken, J.; et al. Giant Electron–Phonon Coupling and Deep Conduction Band Resonance in Metal Halide Double Perovskite. *ACS Nano* **2018**, *12*, 8081–8090. [[PubMed](#)]

38. La-o-vorakiat, C.; Xia, H.; Kadro, J.; Salim, T.; Zhao, D.; Ahmed, T.; Lam, Y.M.; Zhu, J.-X.; Marcus, R.A.; Michel-Beyerle, M.-E.; et al. Phonon Mode Transformation Across the Orthohombic–Tetragonal Phase Transition in a Lead Iodide Perovskite $\text{CH}_3\text{NH}_3\text{PbI}_3$: A Terahertz Time-Domain Spectroscopy Approach. *J. Phys. Chem. Lett.* **2015**, *7*, 1–6. [[CrossRef](#)]
39. Zhang, B.; Klarbring, J.; Ji, F.; Simak, S.I.; Abrikosov, I.A.; Gao, F.; Rudko, G.Y.; Chen, W.M.; Buyanova, I.A. Lattice Dynamics and Electron–Phonon Coupling in Double Perovskite $\text{Cs}_2\text{NaFeCl}_6$. *J. Phys. Chem. C* **2023**, *127*, 1908–1916. [[CrossRef](#)]
40. Verma, A.S.; Kumar, A. Bulk modulus of cubic perovskites. *J. Alloys Compd.* **2012**, *541*, 210–214. [[CrossRef](#)]
41. Chu, W.; Zheng, Q.; Prezhdo, O.; Zhao, J.; Saidi, W.A. Low-frequency lattice phonons in halide perovskites explain high defect tolerance toward electron-hole recombination. *Sci. Adv.* **2020**, *6*, eaaw7453. [[CrossRef](#)] [[PubMed](#)]
42. Yu, Z.-G. Rashba Effect and Carrier Mobility in Hybrid Organic–Inorganic Perovskites. *J. Phys. Chem. Lett.* **2016**, *7*, 3078–3083. [[CrossRef](#)] [[PubMed](#)]
43. Xie, J.; Zhang, Z.Y.; Yang, D.Z.; Xue, D.S.; Si, M.S. Theoretical Prediction of Carrier Mobility in Few-Layer BC_2N . *J. Phys. Chem. Lett.* **2014**, *5*, 4073–4077. [[CrossRef](#)] [[PubMed](#)]
44. Verdi, C.; Giustino, F. Fröhlich Electron-Phonon Vertex from First Principles. *Phys. Rev. Lett.* **2015**, *115*, 176401. [[CrossRef](#)]

Disclaimer/Publisher’s Note: The statements, opinions and data contained in all publications are solely those of the individual author(s) and contributor(s) and not of MDPI and/or the editor(s). MDPI and/or the editor(s) disclaim responsibility for any injury to people or property resulting from any ideas, methods, instructions or products referred to in the content.